aerospace

MDPI

Article

The Impact of Distributed Propulsion on the Aerodynamic Characteristics of a Blended-Wing-Body Aircraft

Wenyuan Zhao , Yanlai Zhang , Peng Tang and Jianghao Wu *

School of Transportation Science and Engineering, Beihang University, Beijing 100191, China
* Correspondence: buaawjh@buaa.edu.cn

Abstract: Motivated by outstanding aerodynamic performance and limited emissions, the blend-wing-body (BWB) aircraft equipped with a distributed propulsion (DP) system has become a possible layout for civil aircraft in the next generation. Due to the strong aero-propulsive interference (API) between the DP system and the airframe, the conventional integration of pressure and friction stress over the surface may fail to evaluate the aerodynamic power consumption of this layout. Here, the aero-propulsive integrated power balance approach is used alternatively to obtain the aerodynamic power consumption through flow data. We demonstrate that the API effects can enlarge both the lift and aerodynamic power consumption of this layout. The increase in power consumption is attributed to the enhanced viscous dissipation rate within the boundary layer. Wind tunnel experiments further demonstrate that the operation of the DP system can improve the stall characteristics. Our findings encourage limiting the inflow speed of the DP system to alleviate the enhancement in viscous dissipation rate and thus reduce the power consumption.

Keywords: distributed propulsion; aero-propulsive interference; aero-propulsive integrated power balance method; flight test; CFD

check for updates

Citation: Zhao, W.; Zhang, Y.; Tang, P.; Wu, J. The Impact of Distributed Propulsion on the Aerodynamic Characteristics of a Blended-Wing-Body Aircraft. *Aerospace* **2022**, *9*, 704. https://doi.org/10.3390/aerospace9110704

Academic Editor: Vittorio Cipolla

Received: 15 September 2022
Accepted: 7 November 2022
Published: 10 November 2022

1. Introduction

The blended-wing-body (BWB) aircraft equipped with distributed propulsion (DP) has gained continued attention due to its obvious potential in improving the performances of aerodynamics, propulsion, flight control, noise, and emissions [1–4]. This configuration is widely used in the concept design of many advanced aircraft [5–7], such as N3-X and SAX-40. A BWB is a wing-body highly integrated aerodynamic layout and its center body part has a larger volume, distinguishing it from the flying wing layout [2]. It possesses the advantages of high aerodynamic efficiency, low emissions, and low noise [2,8–10]. Distributed propulsion (DP) is a propulsion concept in which the propulsion units are distributed and installed in the airframe, changing the way of providing thrust from centralized to distributed, featuring a higher bypass ratio, higher propulsion efficiency, and lower noise [4]. The configuration of the BWB aircraft equipped with a DP system can take advantage of the aero-propulsive interference (API) to improve the overall performance [1,4,11–13].

Theoretical research has shown that the BWB aircraft equipped with a DP system can improve its propulsion efficiency and reduce power consumption due to the effects of boundary layer ingestion (BLI) and wake filling [14–18]. A study evaluating the benefits of BLI on the common research model (CRM) showed that the engine power requirements are reduced by 8% at cruise for the boundary-layer-ingestion configuration when compared to the baseline geometry [17]. A numerical evaluation study showed that BLI achieved power savings of more than 10% on STARC-ABL [18]. Due to the strong API effects, the aerodynamic characteristics of this advanced layout are distinct from those of conventional aircraft [19–24]. A computational investigation of the API effects on a multi-fan system mounted on a simplified wing shows that both the thrust angle and level affect the lift, moment, and drag [19]. Wind tunnel experiments focusing on the complex propulsive-airframe interactions of an overwing DP system with a BLI effect revealed the nonlinear change of streamwise and stream-normal forces and pitching moment over the angle of attack and throttle setting [21]. It was further shown that the nozzle deflection of the electric DP system on a quasi-2D S8036 airfoil led to a significant increase in the stream-normal force and the thrust direction also increases in the overall pitching moment [22]. A wind tunnel study on the API between distributed electric propulsion (DEP) and wing showed that DEP can significantly increase the lift direction force and reduce the streamwise force of the wing [25]. These works considering the API effects, all pointed out the potential of API in increasing the stream-normal force of the DPD. However, the impact of API on the aerodynamic power consumption of the DPD has been discussed less. Moreover, the potential of API effects in improving stall characteristics has also been neglected. When studying the API effects on aerodynamics, propulsion, and control, the accuracy of the computational fluid dynamics (CFD) simulations must be verified through parallel experiments, in which a demonstrator for the BWB aircraft with a DP system is necessary.

In this paper, the aerodynamic characteristics of a typical BWB aircraft with a DP system are studied using both experiments and numerical simulations. Both flight tests and wing-tunnel experiments were conducted to measure the aerodynamic loads and further simulations demonstrated the pressure distribution on the airframe. First, the flight tests and simulations of an 11:1 scaled demonstrator of this configuration were carried out at both gliding and climbing conditions to outline its prestall aerodynamic characteristics. The CFD method was then verified using a comparison with flight tests. Based on the CFD data, the aero-propulsive integrated power balance approach [26] was used to evaluate the aerodynamic power consumption of the scaled demonstrator. Finally, wind tunnel experiments of another 29:1 scaled model were conducted to evaluate the aerodynamic performance of this configuration at large angles of attack, searching for any improvement in stall characteristics. The key findings of this research are summarized in Section 4.

2. Analysis Methods

The effect of distributed propulsion on the aerodynamic performance of a low speed BWB aircraft is analyzed in this paper. Flight test is mainly used to study the influence of DP on the aerodynamic forces of a distributed propulsion demonstrator (DPD) and verify the accuracy of CFD calculations. The flight time of the DPD is limited by the battery capacity, so the test results do not include cruising status results. After the accuracy of the CFD calculation is verified by the flight test, CFD are used for a more detailed aerodynamic power consumption analysis in cruise state. Wind tunnel tests are used to study the stall characteristics of a DPD at high angles of attack because they are safer than flight tests and are closer to real flight conditions than CFD.

In this section, the components and geometric details of the scaled-down distributed propulsion demonstrator (DPD) are first described. Second, the aero-propulsive integrated power balance method [26] used in calculating the aerodynamic power consumption is presented briefly. Then, the setup of CFD simulations is introduced. Finally, the data collection and postprocessing methods in flight tests and the setup of wind-tunnel experiments are explained.

2.1. DPD Model

The DPD consists of a three-dimensional (3D) low-speed BWB airframe and a DP system located around the rear end of the upper surface (Figure 1). The DP system consists of four electric ducted fans, each of which is capable of producing a takeoff thrust of 11.5 kg. The DP system is symmetrically positioned with respect to the central plane of the airframe. Details for the design parameters of the BWB airframe and the geometry of the fans are listed in Table 1.

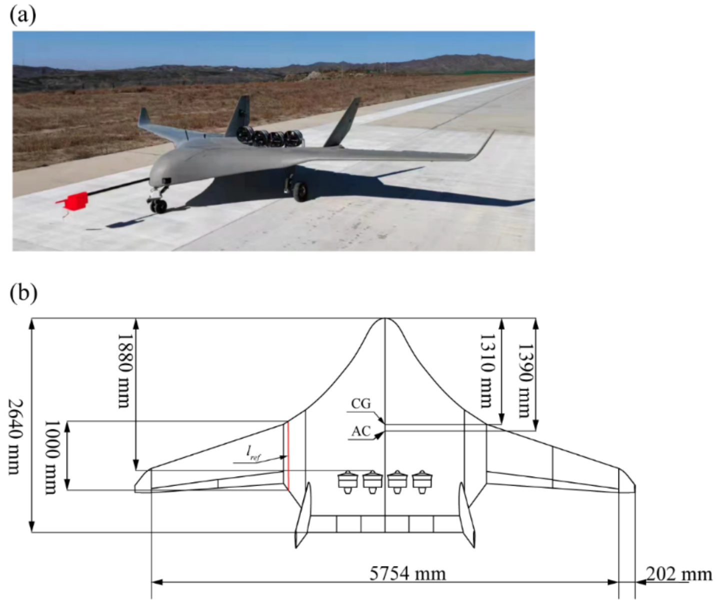

Figure 1. The scaled-down distributed propulsion demonstrator (DPD). (**a**) Actual model for flight tests; (**b**) Schematic diagram showing the geometric parameters of the BWB airframe and the installation position of the fans.

Table 1. Detailed design parameters of the scaled-down DPD.

Parameters	Values
Mass, m/kg	130
Span, b/m	6.1
Reference area, S_{ref}/m^2	5.774
Reference length, L/m	1
Center of gravity, CG/m	1.31
Aerodynamic center, AC/m	1.39
Average aerodynamic chord length, c/m	0.863
Fan length, l_{fan}/m	0.341
Fan inner diameter, D_{in}/m	0.241
Fan outer diameter, D_{out}/m	0.253
Inlet area, A_{in}/m	0.0487
Outlet area, A_{out}/m	0.0322

2.2. *Aero-Propulsive Integrated Power Balance Analysis*

This section introduces the theoretical approach to assessing the aerodynamic power consumption of the DPD. Given that the DPD experiences a strong API, a method of power balance of the flow field was applied to evaluate the aerodynamic power consumption of the DPD, instead of the traditional thrust drag bookkeeping method. The aerodynamic power consumption in cruising is employed as an indicator of efficiency, and the smaller the aerodynamic power consumption is, the higher the aerodynamic efficiency is. Our aero-propulsive integrated power balance analysis follows the work of Drela [26], which derives the power balance equation applicable to the low-speed flow field. The decomposition and subcalculation of the total aerodynamic dissipation of the aircraft, as well as the method of analyzing the strength of local dissipation, were also introduced in Drela [26].

2.2.1. Power Balance in Low-Speed Flow Fields

A control volume v is constructed to analyze the power balance of the flow field around the DPD. The inner boundary S_B of the control volume covers the BWB surface and the inlet and outlet planes of the DP system. The outer boundary S_o is placed in the far field where the free flow conditions are satisfied (usually places S_o several characteristic lengths of the aircraft away from S_B), and the normal direction of S_o points out of the control volume (Figure 2).

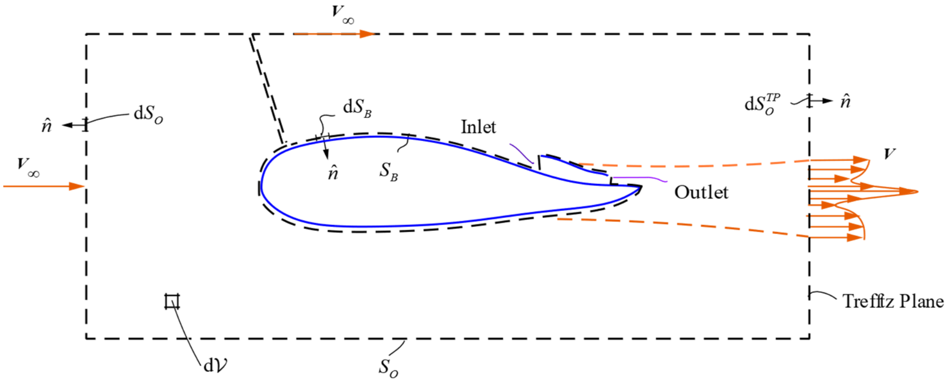

Figure 2. Two-dimensional (2D) cross-section of the control volume v for power balance analysis.

Assuming that the flow is fully steady, the power balance in the control volume can be expressed as

$$P_K = -F_X V_\infty + \Phi_\infty - P_V \tag{1}$$

where P_K represents the input power of the DP system into the flow field; F_X represents the net streamwise force acting on the DPD, i.e., the balance of the drag of the BWB airframe and the thrust of the DP system; V_∞ represents the freestream velocity; $-F_X\ V_\infty$ represents the power consumed or provided by changing the gravitational potential energy when the aircraft deviates from cruising; Φ_∞ represents the viscous dissipation rate in the control volume; and P_V represents the volume power of pressure in the control volume, which is negligible in a low-velocity flow. The terms in Equation (1) are defined as follows:

$$P_K = \oiint\limits_{S_B} -\left[(p - p_\infty) + \frac{1}{2}\rho\left(V^2 - V_\infty^2\right)\right]\mathbf{V}\cdot\hat{n}dS \tag{2}$$

$$F_X = \oiint\limits_{S_B} -[(p - p_\infty)\hat{n} - \boldsymbol{\tau} + \rho \mathrm{V} V_n]\cdot\hat{\mathrm{e}}_X dS \tag{3}$$

$$\Phi_\infty = \iiint\limits_{v} (\boldsymbol{\tau}\cdot\nabla)\cdot \mathrm{V}d\mathrm{v} \tag{4}$$

2.2.2. Decomposition of Viscous Dissipation Rate

The viscous dissipation in the flow field occurs mainly in the boundary layer and the wake of the BWB airframe, the jet region of the DP system, and the trailing-edge vortex (Figure 3). The viscous dissipation rate Φ_∞ can be thus decomposed into four subterms according to the regions where the dissipation occurs

$$\Phi_\infty = \Phi_{bl} + \Phi_{wake} + \Phi_{vortex} + \Phi_{jet} \tag{5}$$

where the trailing-edge vortex loss rate Φ_{vortex} is associated with lift; the boundary layer loss rate Φ_{bl} and subsequent wake loss rate Φ_{wake} are related to the shape of the BWB airframe; and the jet loss rate Φ_{jet} is related to the jet of the DP system. The combination of Φ_{bl} and Φ_{wake} corresponds to the profile dissipation rate of the BWB airframe Φ_p

$$\Phi_p = \Phi_{bl} + \Phi_{wake} \tag{6}$$

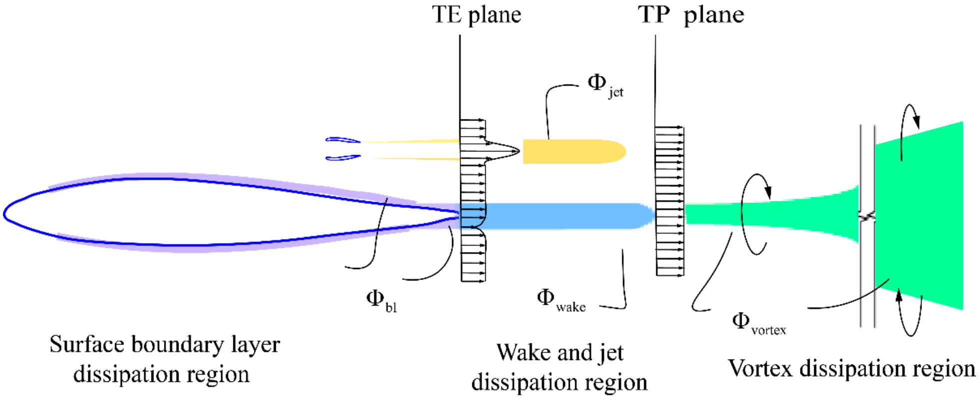

Figure 3. Viscous dissipation in different viscous regions.

The power balance relationship in Equation (1) is derived by placing the plane TP at a downstream position where all dissipation processes have been completed. If the plane TP is placed forward, for example, towards the exit of the DP system, the mixing dissipation of the jet has not yet started at this position, and the mechanical energy still exists in the plane TP in the form of perturbative mechanical energy. Therefore, the mixing dissipation rate of the jet Φ_{jet} can be calculated by integrating the perturbation energy deposited in the jet region in the plane TP

$$\Phi_{jet} = \iint\limits_{jet-plane} \frac{1}{2}\rho(V_i - V_\infty)^2 V_n dS \tag{7}$$

where V_i is the jet velocity assuming an isentropic expansion to the ambient pressure.

The trailing-edge vortex dissipation rate Φ_{vortex} is calculated by placing the plane TP at a downstream position where the pressure recovers to the ambient pressure. At this point, the boundary layer and subsequent wake dissipation have been completed. The only perturbation energy deposited in the plane TP is the energy contained in the trailing-edge vortex.

$$\Phi_{vortex} = \iint\limits_{TP} \frac{1}{2}\rho\left(v^2 + w^2\right)V_n ds \tag{8}$$

2.2.3. Dissipation Distribution in Boundary Layer and Wake

The profile dissipation rate Φ_p occurs in the boundary layer of the airframe surface and the subsequent wake. To monitor the strength of the local dissipation rate in the surface boundary layer, a local coordinate system in the airframe boundary layer and the wake is established. In the local coordinate system of the airframe boundary layer, axes x and z are located on the airframe surface, and axis y is perpendicular to the airframe surface (across the boundary layer). In Figure 4, u and w represent the local velocity components in the x and z directions, respectively.

Neglecting the spanwise flow in the boundary layer (w = 0), Equation (4) for the viscous dissipation rate Φ can be simplified as

$$\Phi = \iiint \tau_{xy}\frac{\partial u}{\partial y}dxdydz \tag{9}$$

Integrating the integrand in Equation (9) along the normal direction of the boundary layer (y) then gives

$$\phi(x,z) = \int \tau_{xy}\frac{\partial u}{\partial y}dy \tag{10}$$

and

$$\Phi = \iiint \phi(x,z)dxdz \tag{11}$$

where $\phi(x, z)$ illustrates the distribution of local dissipation rate on the aircraft surface. By comparing the values of $\phi(x, z)$ at typical locations, targeting the region that causes an increase in the profile dissipation rate Φ_p of the airframe is possible.

Φ_p can be further decomposed as the product of two terms

$$\phi(x,z) = \frac{1}{2}\rho u_e^3 C_\phi \tag{12}$$

Thus, the local dissipation rate $\phi(x, z)$ is determined by the velocity at the outer edge of the boundary layer u_e and the local dissipation rate coefficient C_Φ. The former is influenced by the local pressure gradient, and the latter is related to the shape of the boundary layer.

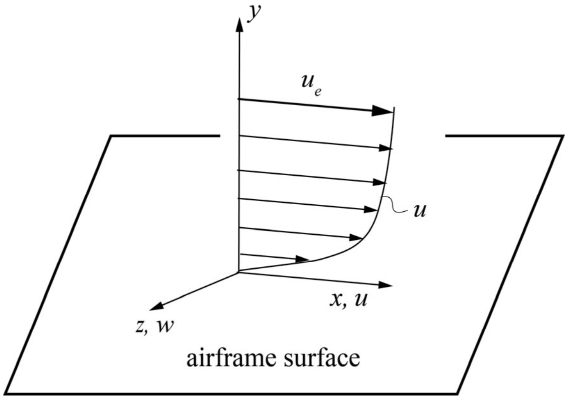

Figure 4. The local coordinate system of the airframe boundary layer.

2.3. CFD Simulation

2.3.1. Solver Setups

The control equations of the flow field in this paper are three-dimensional, constant, and incompressible RANS equations. A pressure-based solver is used to solve the control equations with second-order spatial accuracy, and the turbulence model involved is the S-A one-equation model. Given the freestream velocity, the velocity inlet condition is used for the far-field boundaries. The symmetric plane of the model is set as a symmetric boundary condition. No-slip wall boundary conditions are imposed on all surfaces of the DPD. The velocity inlet condition is also used for the inlet and outlet of the DP system, which is equivalent to setting the mass flow rate since the flow field is uncompressible. The inlet V_{in} and outlet V_{out} speeds of the DP system are obtained by the following one-dimensional relational equation

$$P_K = \frac{1}{2}\rho V_{jet} A_{jet}\left(V_{jet}^2 - V_\infty^2\right) \tag{13}$$

$$\dot{m} = \rho V_{jet} A_{jet} = \rho V_{in} A_{in} \tag{14}$$

Using Equations (13) and (14), the speed of the inlet and outlet of the DP system can be calculated under a given power.

2.3.2. Mesh Setups

In this paper, the longitudinal aerodynamic characteristics of the DPD are studied, and thus the flow field is symmetric about the symmetric plane. Therefore, the numerical simulation is carried out using a half-mode C–H type mesh. The domain size is 40 times of the root chord length c_{root} from the aircraft in each direction to ensure the feasibility of the far-field boundary conditions. The height of the first grid layer above the wall is 1.2×10^{-5} m, ensuring the requirement for the S-A model $y^+ \leq 1$. The mesh of the symmetry plane is shown in Figure 5.

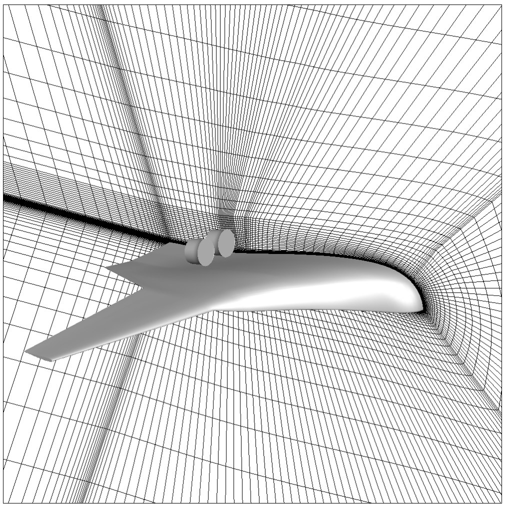

Figure 5. Computational mesh for the CFD simulations.

2.4. Flight Test

2.4.1. Conditions and Data Collection

The flight test aims to evaluate the impact of the API of the DP system on the aerodynamic force of the BWB aircraft under a full-engine throttle climb and a small power glide. The maximum field height is 130 m, and the maximum flight speed is 125 km/h. The inertial navigation system in the onboard system incorporates GNSS signals to obtain the attitude angle, flight speed, position, and other flight parameters. The atmospheric data sensor in the onboard system measures the total and static pressure on the surface of the aircraft and the nearby area, and thus obtains the flight altitude after being solved by the atmospheric data computer. The atmospheric data sensor also integrates the angle of attack and sideslip measurement devices. The accuracy of the atmospheric data sensor used in this validator is less than 0.5° for the angle of attack and the sideslip angle, and the measurement range can meet the test requirements. In addition, the electronic governor of the power system can record the voltage and current parameters during the flight.

2.4.2. Data Postprocessing

In this section, the center-of-mass motion of the DPD is analyzed in the ground coordinate system $Ox_gy_gz_g$ and the trajectory coordinate system $Ox_ky_kz_k$. The overall aerodynamic forces are obtained implicitly by solving the equations of dynamics. The definition of the two coordinate systems is shown in Figure 6. In the ground coordinate system $Ox_gy_gz_g$, the axis Ox_g points in any selected direction in the horizontal plane H; the axis Oz_g points to the ground vertically; the axis Oy_g is perpendicular to the plane Ox_gz_g, and the direction is determined by the right-hand rule. In the trajectory coordinate system $Ox_ky_kz_k$, the axis Ox_k points in the direction of ground speed V_k; the axis Oz_k is located in the vertical plane V, perpendicular to the axis Ox_k, and pointing to the ground; the axis Oy_k is perpendicular to the plane Ox_kz_k, and the direction is determined by the right-hand rule. The relationship of $Ox_gy_gz_g$ and $Ox_ky_kz_k$ is thus described by the trajectory orientation angleχ and the trajectory inclination angleγ. χ refers to the angle between the projection of V_k on the horizontal plane H and the axis Ox_g. γ is the angle between V_k and the horizontal plane H.

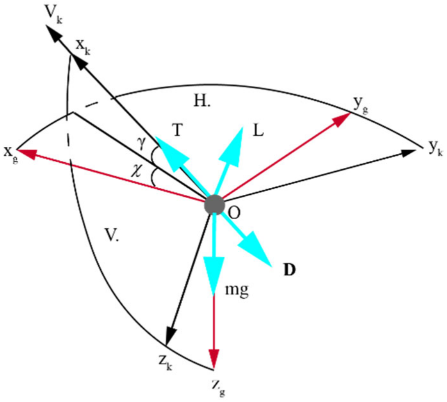

Figure 6. Coordinate system definition in flight tests.

Since the longitudinal motion of the DPD is analyzed, the lateral and transverse motions of the DPD are ignored. The longitudinal kinematic equations of the DPD in the ground coordinate system $Ox_gy_gz_g$ are presented as follows:

$$\begin{aligned} \frac{\mathrm{d}x_g}{\mathrm{d}t} &= V_k \cos\gamma \\ \frac{\mathrm{d}z_g}{\mathrm{d}t} &= -V_k \sin\gamma \end{aligned} \tag{15}$$

The derivation of Equation (15) yields

$$\begin{aligned} \frac{\mathrm{d}}{\mathrm{d}t}\left(\frac{\mathrm{d}x_g}{\mathrm{d}t}\right) &= \frac{\mathrm{d}V}{\mathrm{d}t}\cos\gamma - V\sin\gamma\frac{\mathrm{d}\gamma}{\mathrm{d}t} \\ \frac{\mathrm{d}}{\mathrm{d}t}\left(\frac{\mathrm{d}z_g}{\mathrm{d}t}\right) &= \frac{\mathrm{d}V}{\mathrm{d}t}\sin\gamma + V\cos\gamma\frac{\mathrm{d}\gamma}{\mathrm{d}t} \end{aligned} \tag{16}$$

The airflow coordinate system is identical to the trajectory coordinate system $Ox_ky_kz_k$ when the transverse and lateral motions are ignored. Thus, the propulsion thrust T is parallel to Ox_k and takes the same direction as Ox_k; aerodynamic drag D is parallel to Ox_k but opposite to Ox_k; the aerodynamic lift L is parallel to Oz_k but takes an opposite direction; the gravity mg is parallel to Oz_g and takes the same direction as Oz_g. The longitudinal dynamic equations of the DPD in the trajectory coordinate system $Ox_ky_kz_k$ are thus derived as follows:

$$\begin{aligned} m\frac{\mathrm{d}V}{\mathrm{d}t} &= T - D - mg\sin\gamma \\ -mV\frac{\mathrm{d}\gamma}{\mathrm{d}t} &= -L + mg\cos\gamma \end{aligned} \tag{17}$$

The data recorded by the onboard system include the time series of dz_g/dt and V_k, and their derivatives $d(dz_g/dt)/dt$ and dV_k/dt can be thus obtained using the finite difference method. Bringing these variables into Equations (15) and (16), then obtaining γ and $d\gamma/dt$, and takingγ, $d\gamma/dt$, V_k, and dV_k/dt into Equation (17) gives the aerodynamic lift L and the streamwise net force F_x ($F_x = T - D$).

2.4.3. Ground Test for the DP System

The mechanical power input to the flow field of the propulsion system P_{K} represents the operation status of the DP system. In this paper, the electric ducted fan is selected for the propulsion system, and the mechanical power provided by the propulsion system can be calculated by the following equation,

$$P_K = P_E\eta \tag{18}$$

where P_E is the electric power consumed by the propulsion system, and η is the motor efficiency of the DP system.

The electronic governor carried by the DP system can record the driving voltage V and current I of the DP system during flight, and their product corresponds to the electrical power P_E consumed by the propulsion system. To estimate the mechanical power P_K provided by the propulsion system during flight, the motor efficiency η in Equation (18) should be preknown. Here, η was first obtained through ground tests for the DP system. In the ground tests, the DP system is mounted on a carrier and experiences different freestream velocities V_{k}. The driving current I and voltage V of the DP system and the mechanical power P_K generated by the DP system are recorded V_{k}, and the motor efficiency η at different V_{k} are thus calculated by Equation (18). Therefore, a database η = (P_E, V_{k}) is established, as plotted in Figure 7. Note that the numbers on the data lines inform the V_{k}.

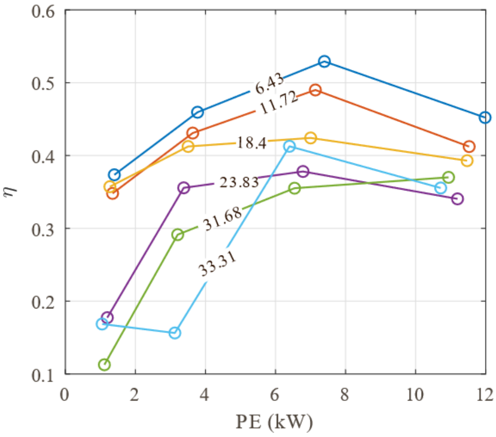

Figure 7. Motor efficiency database for the DP system.

The motor efficiency η of the propulsion system is assumed to be identical in both flight tests and ground tests as long as the electrical drive power P_E and freestream velocity V_{k} are the same. Thus, the motor efficiency η in flight tests can be obtained by interpolating from the database η = (P_E, V_{k}), and the mechanical power P_{K} can be calculated according to Equation (18).

2.5. Wind Tunnel Experiments

The wind tunnel experiments were performed in a 3.5 m × 2.5 m, low-speed, single-closed-return wind tunnel, with a test speed of up to 73 m/s. The average turbulence intensity of the experimental section was 0.19%. The scaled-down DPD (Figure 8) had some trivial modifications around the rear part of the airframe, and the scaling ratio was (3.4%). The span length of this DPD was 2.29 m and the scaled DP system consisted of six ducted fans, the diameters all of which were 0.09 m. The maximum thrust of the scaled fan was 50 N, corresponding to a maximum intake mass-flow rate of 0.701 kg/s, and the maximum jet speed was 90 m/s.

Figure 8. The scaled-down DPD in the wind tunnel experiments.

A six-component balance was used to measure the streamwise and stream-normal forces (C_X and C_L) and pitching moment of the model. The streamwise and stream-normal forces were used to define the forces produced by the model because the standard decoupled definitions of lift, drag, and thrust on this aero-propulsive coupled model were ambiguous. The model was mounted on a single strut support, which was at the middle of the abdomen surface, and the relative position of the strut and the model was fixed. The correction of support interference was carried out by a two-step method using the dorsal support as an auxiliary support. Moreover, the model and the strut were then fixed on a curved track in the wind tunnel to change the angle of attack.

3. Results and Discussion

3.1. Impact of DP on the Prestall Aerodynamic Forces of the DPD

To analyze the impact of the API effect of the DP system on the prestall aerodynamic force of the DPD, two typical statuses were selected within the flight envelope, i.e., the climbing state with a large mass flow rate and the gliding state with a small mass flow rate. Due to the limited capacity of the battery, the DPD could not fly for a long time, so there was no cruise result in the flight test. Despite this, the difference in mass flow rate between the climbing state and the gliding state is obvious, and their comparison can illustrate the change in aerodynamic force caused by the API effect of the DP system. In addition, this comparison of the results obtained by flight tests and CFD simulations can also verify the accuracy of our CFD setup. After verifying that the CFD calculation results were consistent with the test flight results, subsequent studies were carried out using CFD, focusing on the aerodynamic power consumption at cruise state.

In the CFD simulations, the lift force L was obtained by integrating the pressure and friction forces on the BWB airframe surface and projecting them in the vertical streamwise direction, while the streamwise force F_{X} was calculated using Equation (3), including the BWB airframe surface and the DP system inlet and outlet planes. The DP system input power P_{K} was calculated by Equation (2), and the integration was over the inlet and outlet planes of the DP system. In discussion, L and F_{X} were normalized by $1/2\rho V_{\infty}^{2}S_{ref}$ and P_{K} was normalized by $1/2\rho V_{\infty}^{2}S_{ref}$. The input power coefficient C_{PK} of the two typical statues is shown in Table 2, and the corresponding aerodynamic force coefficients C_{L} and C_{X} are shown in Figure 9. Here, "climb" and "glide" represent the results of the climbing and gliding statuses; "exp" and 'cfd' distinguish the results from flight tests and CFD simulations.

Table 2. C_{PK} of the DPD aircraft at climbing and glide conditions.

Labels	C_{PK}
climb-exp	0.100
climb-cfd	0.097
glide-exp	0.008
glide-cfd	0.007

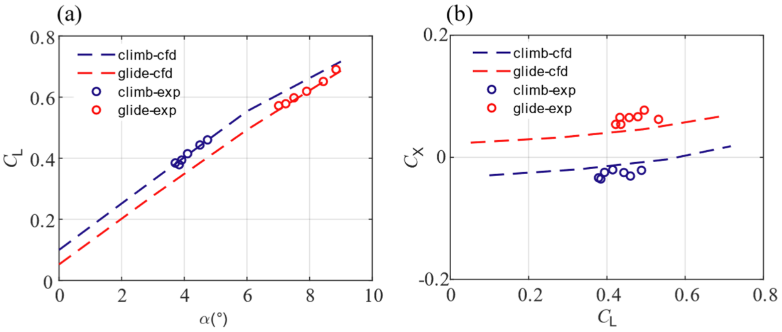

Figure 9. (**a**) C_L-α, (**b**) C_X-C_L.

In Table 2, the values of C_{PK} obtained from flight tests and CFD simulations are close under the same flight condition, indicating that the operating state of the DP system simulated by CFD is consistent with that in the flight test. The C_{L}-α curves of the DPD aircraft under climbing and gliding conditions (Figure 9a) further verified the accuracy of the CFD simulations. Compared to the flight test data, the error of C_{L} in the CFD calculation is within 5%. More importantly, the API effect of the DP system significantly increased the C_{L} at any angle of attack α. In the climbing status where the mass flow rate of the DP system was higher, the APL effect (manifested as the BLI effects) was strong compared to that in the gliding state where the mass flow of the DP system was lower. Within the range of the prestall α, the average increase in C_{L} with strong API effects was 0.05 compared to that with weaker API effects, which was about 13% of the value of C_{L} in cruise (0.38, calculated from the balance of lift and gravity of the aircraft at cruising state). According to Figure 9b, a slight discrepancy of C_{X} was observed between the CFD simulations and the flight tests, which may be attributed to the error in α measurement in the flight tests and the fact that the CFD simulations were performed under full turbulence conditions (turbulent viscosity ratio was set to 1). This may be different from the actual flow field. The Reynolds numbers with the wing root chord length and wing tip chord length as the reference length were 4.8×10^6 and 6×10^5, respectively. Due to safety concerns, the flight test had the angle of attack protection, and the test could not be carried out at a high angle of attack.

3.2. Impact of the DP System on the Viscous Dissipation Rate of the DPD

In the analysis of aerodynamic power consumption, the landing gear, winglet, and vertical tail that are far from the DP system were removed from the simplified models since the operation of the DP system had less influence on these components. The difference in C_{X} between the simplified model and the complete model was about -0.0149 at the same C_{L} and C_{PK}. In this section, four simplified models for the DPD (Figure 10) are simulated. Model A1 and A2 both had a noninstalled DP system. The DP system of A1 was set at a through-flow condition while that of model A2 was powered up. The conditions of the DP system of models B1 and B2 were identical to that of A1 and A2, respectively, while the DP system was mounted to the BWB airframe. Here, the noninstalled DP system meant that the airframe and the DP system were simulated separately, and the flow fields of the two components did not interact with each other. The impact of the installation of the DP system on the aerodynamic power consumption of the DPD could be evaluated through a comparison between A1 and B1. In contrast, the impact of the operation state of the DP system on the aerodynamic power consumption of the DPD could be analyzed through a further comparison between A2 and B2.

The aerodynamic disturbances caused by the DP system installation were evaluated first through a comparison between B1 and A1. The aerodynamic forces of the BWB airframe and the DP system of A1 were first calculated separately and then summed to obtain the total values. The statues for comparison were set at $\alpha = 5^\circ$ and $C_{\mathrm{L}} = 0.38$. The total aerodynamic dissipation rate Φ_∞ was obtained indirectly by Equation (1) and then decomposed into Φ_{p} and Φ_{v} by Equations (5) and (8), respectively. Φ_{jet} was set to zero because no fan was powered in the through-flow models. The dissipation rate components were then normalized by $1/2\rho V_\infty^2 S_{ref}$ to obtain their corresponding coefficients listed in Table 3.

Table 3. Comparison of the aerodynamic dissipation rate components.

	α	C_{X}	C_{PK}	$\mathbf{C}_{\mathbf{\Phi}}^{\infty}$	$\mathbf{C}_{\mathbf{\Phi}}^{\mathbf{v}}$	$\mathbf{C}_{\mathbf{\Phi}}^{\mathbf{jet}}$	$\mathbf{C}_{\mathbf{\Phi}}^{\mathbf{p}}$
A1	5	0.0329	−0.0020	0.0309	0.0106	-	0.0203
B1	5	0.0326	−0.0025	0.0301	0.0104	-	0.0197
A2	5	−0.0145	0.0580	0.0435	0.0109	0.0114	0.0212
B2	4	−0.0134	0.0655	0.0521	0.0105	0.0158	0.0258

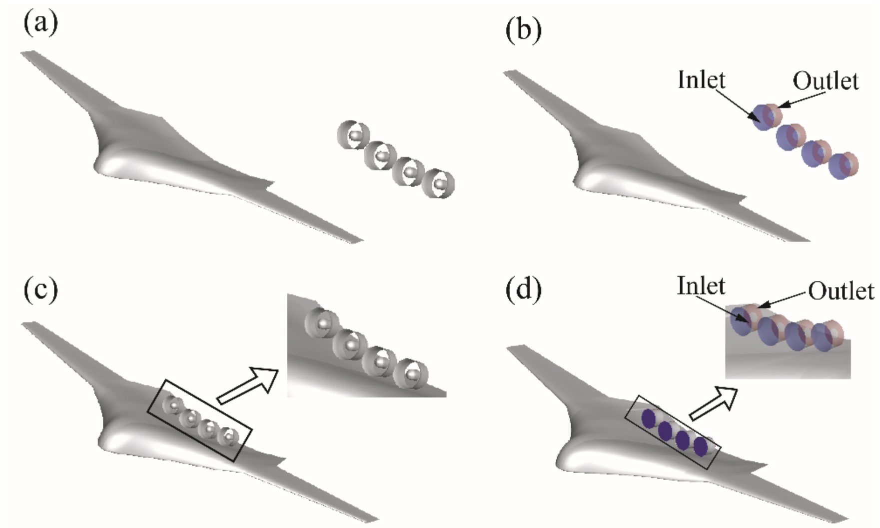

Figure 10. Simplified models of DPD for the analysis of aerodynamic power consumption. (**a**) Noninstalled through-flow model A1; (**b**) Noninstalled with powered fans model A2; (**c**) Mounted through-flow model B1; (**d**) Mounted with powered fans model B2.

As shown in Table 3, the total dissipation rates C_{Φ}^{∞} of A1 and B1 were almost the same, with a difference of only 0.0008, 75% which was from the difference in $\mathbf{C_{\Phi}^{p}}$ and 25% from the difference in $\mathbf{C_{\Phi}^{v}}$. Therefore, the installation of the DP system has minimal effect on the aerodynamic dissipation rate of the DPD. Afterward, the effect of the DP system operation on the dissipation rates of the DPD was analyzed through A2 and B2, both of which had powered fans in the DP system. The analysis was conducted under the cruise condition (i.e., $C_L = 0.38$ and $C_X = -0.0149$) and the negative C_X was chosen to balance the drag of the components that were not involved in simplified models. The aerodynamic forces and dissipation rate were calculated in the same way as the through-flow condition. The jet loss Φ_{jet} was calculated using Equation (7) with the integration plane placed at the exit of the DP system.

As shown in Table 3, at the cruise condition, the total aerodynamic dissipation rate coefficient C_{Φ}^{∞} of B2 was remarkably higher than that of A2. The dissipation rate decomposition in Table 3 shows that half of the increase in C_{Φ}^{∞} came from the increase in $C_{\Phi p}$ and the other half came from the concomitant increase in C_{Φ}^{jet} These results are different from those of the propulsion airframe configuration which showed that the boundary layer dissipation did not change significantly with BLI [15,27]. The increased C_{Φ}^{p} in B2 may be caused by the interaction between the aerodynamic outer flow around the BWB airframe and the propulsive inner flow of the DP system. According to the power balance equation (Equation (1)), if an identical value of C_X is obtained by B2 with A2, the input power coefficient C_{PK} of B2 should be enlarged to balance the increase in C_{Φ}^{p}, and thus the jet velocity V_{jet} is enlarged within a constant outlet area, which leads to the increase in C_{Φ}^{jet}.

Furthermore, the distribution of the surface friction (C_f) near the inlet of the DP system was compared between A2 and B2 to explain the increase in C_{Φ}^{p}. As shown in Figure 11, the red and blue areas outline the regions with a large and low local dissipation rate, respectively. The surface friction in front of the DP system inlet of B2 was significantly larger than the local surface friction of A2. The streamwise range of the enlarged surface friction was about the DP system length, which encountered a strong API.

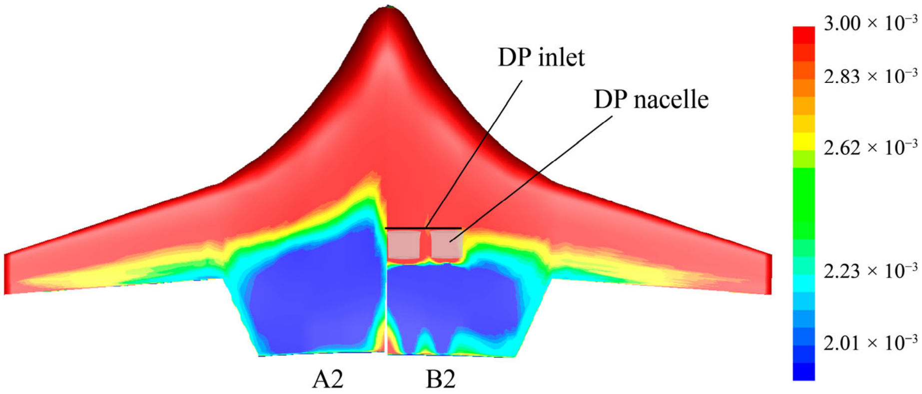

Figure 11. Comparison of the distribution of surface friction coefficient C_f.

To further relate this strong surface friction ahead of the DP system with the streamwise velocity in the boundary layer, the local velocity profiles in the boundary layers of A1, B1, and B2 were compared (Figure 12a) and the resulting velocity gradients in the normal direction $\partial u/\partial y$ were calculated in Figure 12b. Compared to A1, the simplified model B1 and B2 generated a flatter velocity profile at the inlet of the DP system, and thus the near-wall velocity gradients of B1 and B2 increased significantly (Figure 12b). This resulted in a strong local dissipation rate ϕ according to Equation (10).

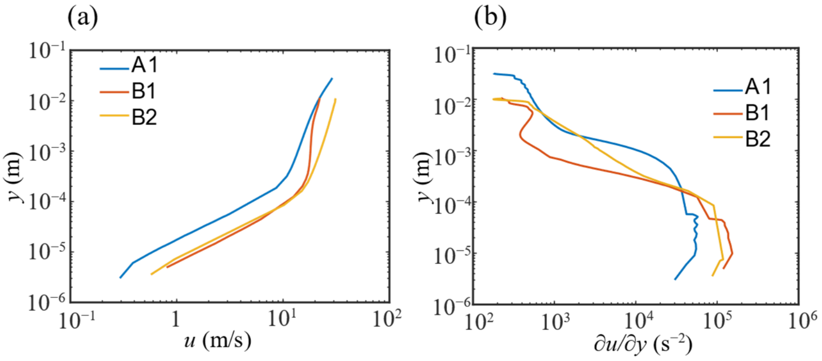

Figure 12. Comparison of the velocity profiles (**a**) and the velocity gradients (**b**) in the boundary layer at the DP system inlet of A1, B1, and B2.

The local dissipation rates ϕ at the DP system inlet of A1, B1, and B2 were then decomposed into $0.5\rho u_e^3$ and C_Φ using Equation (12), as shown in Table 4. The value of ϕ at the DP system inlet of B1 was similar to that of A1, which was consistent with the comparison results of the total dissipation rate Φ_∞ (Table 3). However, the value of ϕ at the DP system inlet of B2 was twice that of A1, indicating that the stronger dissipation rate of B2 was strongly related to the API effect. The decomposition results in Table 4 further show that the variation in $0.5\rho u_e^3$ was the dominant factor of the change in ϕ. This phenomenon may be due to the fact that the high mass flow rate of the DP system increased the flow velocity around the installation location, which thus increased the velocity on the outer edge of the boundary layer and the local dissipation ϕ. Therefore, it is suggested that an improved design of the DP system should reduce the speed at the inlet to decrease local ϕ.

Table 4. Decomposition of local dissipation rates ϕ.

	$\Phi(x, y)$ (kg/s^3)	**$0.5\rho u_e^3$(kg/s^3)**	**C_Φ**
A1	46.7	1.96×10^4	0.0024
B1	51.8	1.53×10^4	0.0034
B2	99.7	3.23×10^4	0.0031

3.3. Improvement of Stall Characteristics of a DPD at Poststall Angles of Attack

Wind tunnel experiments were further conducted to demonstrate the stall characteristics of the DPD at large angles of attack. Here, the nozzle pressure ratio (NPR) of the fan, defined as the ratio of total pressure of the fan outlet flow to the ambient pressure, was employed to represent the throttle statuses and all six fans operate at a uniform NPR level in each test. We defined the state "low throttle" in which the NPR was 1.008. and we also defined the state "high throttle" in which the NPR was 1.029. Each measurement was repeated two times to remove any random error.

Figure 13 shows the stream-normal force coefficient C_L versus the change of angle of attack α for both throttle statuses. The curve named "clean-airframe" corresponded to the clean BWB airframe of the DPD, serving as the baseline case for subsequent comparisons. The throttle status named "low throttle" was used to determine the minimum values of NPR in gliding flight when the fans were installed in the nacelles to avoid a dangerous stall. It was different from the windmilling state, in which no input power was applied to the fans. The throttle status named "high throttle" corresponded to the climbing flight of the DPD, which simulated the operation state of the DP system under strong API effects. Thus, a comparison between "low throttle" and "high throttle" could demonstrate how the stall characteristics of the model were changed by the DP system.

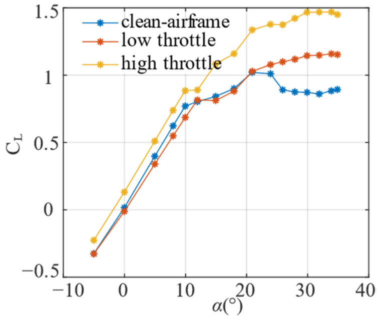

Figure 13. Comparison of the $C_L - \alpha$ curves at two throttle statuses.

As shown in Figure 13, the stall angle of attack $\alpha_{\max}$ of "clean-airframe" was approximately 21°, and the maximum stream-normal force coefficient $C_{\text{L-max}}$ was about 1.02. As α further increased into the poststall range, the increase of C_L was leveled off and then remained around 0.9 since $\alpha > 25°$. However, at $\alpha = 12°$, the C_L at the "high throttle" only experienced a short plateau period and then continued to increase withα. The stall angle of attack $\alpha_{\max}$ of "high throttle" was about 30°, which was 9° larger than that of "clean-airframe". The $C_{\text{L-max}}$ of "high throttle" was about 1.47, which was 0.45 larger than that of "clean-airframe", leading to a stall lift enhancement of over 47%. These results show that the API effects of the DP system can remarkably increase the values of $\alpha_{\max}$ and $C_{\text{L-max}}$ of the scaled-down DPD model, which is useful for improving stall performance.

To monitor the flow separation of the scaled-down DPD, some fluorescence minitufts were pasted to the upper surface in the experiments of three statuses. Two angles of attack were selected for analysis (18° and 35°). The shorter the length of the fluorescent minituft, the more violent the minituft was, which indicated a more serious flow separation. Moreover, the constant length of the minituft indicated that the local flow was attached. Figure 14a–d show that both the "low throttle" and "clean airframe" experienced surface separation at the central plane, indicating that this throttle status led to trivial improvement in the stall characteristics and was reasonable as the minimum operating throttle of the DP system to ensure safety. Figure 14c–f illustrate that the "high throttle" status alleviated the spanwise flow on the upper surface and the flow separation around the central plane, especially at an angle of attack of 35°. The suppression of separated flow on the upper surface of the" high throttle" status explains how the API effects of the DP system improve the stall characteristics of the scaled-down DPD.

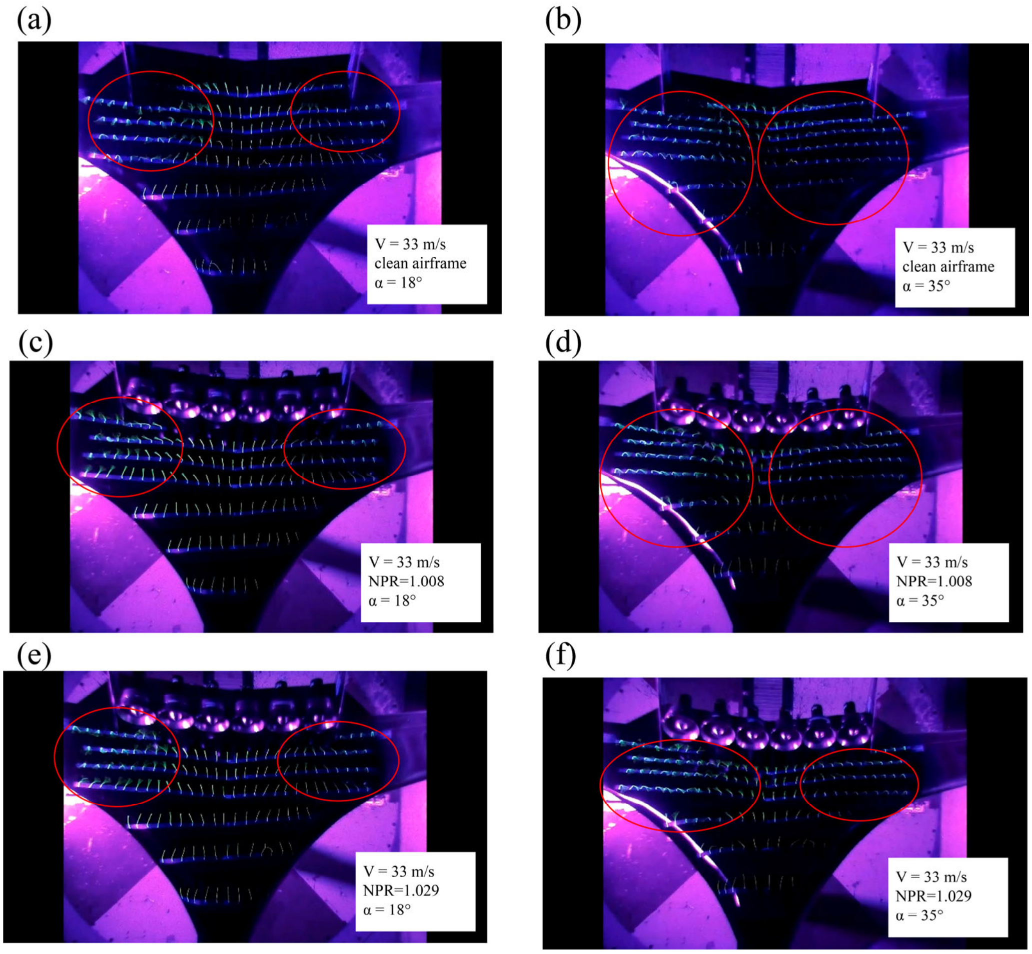

Figure 14. Fluorescent minituft pictures of the wind tunnel experiments. (**a**) "clean airframe" at $\alpha = 18°$; (**b**) "clean airframe" at $\alpha = 35°$; (**c**) NPR = 1.008 at $\alpha = 18°$; (**d**) NPR = 1.008 at $\alpha = 35°$; (**e**) NPR = 1.029 at $\alpha = 18°$; (**f**) NPR = 1.029 at $\alpha = 35°$.

4. Conclusions

In this paper, the aero-propulsive interference (API) effects led by the distributed propulsion (DP) on scaled-down blended-wing-body (BWB) airframes were examined using both simulations and experiments. The aerodynamic forces of an 11:1 scaled-down DP demonstrating aircraft (DPD) were compared between CFD simulations and flight tests, confirming the accuracy of our numerical setup. Based on the CFD data, the aero-propulsive integrated power balance approach was used to evaluate the aerodynamic power consumption of the aircraft. In addition, wind tunnel experiments were conducted to examine the stall characteristics of the aircraft at large angles of attack. Results show that the API effect of the DP system can significantly increase the lift coefficient and the overall power consumption of the aircraft. The lift coefficient of an aircraft with strong API increased by 0.05 compared to one with a weak API, which was approximately 13% of the cruise lift coefficient (0.38). The high-speed inflow of the DP system enlarges the normal gradient of the streamwise velocity within the boundary layer, which thus improves the viscous dissipation rate of the boundary layer. For the stall characteristics, the DP system can increase the critical angle of attack that triggers the stall, and the maximum lift capacity of the aircraft is improved by over 47%. Additionally, not only is the maximum lift coefficient improved, but the overall lift coefficient of the high-throttle model is high throughout the test range. These findings may provide further insights into the aerodynamic power consumption of a BWB airframe with a DP system, giving suggestions for future designs.

Author Contributions: Conceptualization, W.Z., J.W. and Y.Z.; methodology, W.Z. and Y.Z.; software, W.Z.; validation, P.T.; formal analysis, W.Z. and Y.Z.; writing—original draft preparation, W.Z.; writing—review and editing, Y.Z. and J.W.; supervision, J.W.; funding acquisition, J.W. All authors have read and agreed to the published version of the manuscript.

Funding: This research received no external funding.

Data Availability Statement: The data used to support the findings of this study are available from the corresponding author upon request.

Acknowledgments: The authors would like to thank Haotian Zhu and Yang Feng for their help in flight tests and Mancang Gu for his help in reviewing and editing the manuscript.

Conflicts of Interest: The authors declare no conflict of interest.

References

1. Kim, H.D.; Perry, A.T.; Ansell, P.J. A Review of distributed electric propulsion concepts for air vehicle technology. In Proceedings of the 2018 AIAA/IEEE Electric Aircraft Technologies Symposium, Cincinnati, OH, USA, 12–14 July 2018.
2. Okonkwo, P.; Smith, H. Review of evolving trends in blended wing body aircraft design. *Prog. Aerosp. Sci.* **2016**, *82*, 1–23. [CrossRef]
3. Brelje, B.J.; Martins, J.R.R.A. Electric, hybrid, and turboelectric fixed-wing aircraft: A review of concepts, models, and design approaches. *Prog. Aerosp. Sci.* **2019**, *104*, 1–19. [CrossRef]
4. Sahoo, S.; Zhao, X.; Kyprianidis, K. A Review of Concepts, Benefits, and Challenges for Future Electrical Propulsion-Based Aircraft. *Aerospace* **2020**, *7*, 44. [CrossRef]
5. Alrashed, M.; Nikolaidis, T.; Pilidis, P.; Jafari, S. Utilisation of turboelectric distribution propulsion in commercial aviation: A review on NASA's TeDP concept. *Chin. J. Aeronaut.* **2021**, *34*, 48–65. [CrossRef]
6. Hall, C.A.; Crichton, D. Engine Design Studies for a Silent Aircraft. *J. Turbomach.* **2007**, *129*, 479–487. [CrossRef]
7. Felder, J.; Kim, H.; Brown, G. Turboelectric distributed propulsion engine cycle analysis for hybrid-wing-body aircraft. In Proceedings of the 47th AIAA Aerospace Sciences Meeting including The New Horizons Forum and Aerospace Exposition, Orlando, FL, USA, 5–8 January 2009.
8. Liebeck, R.H. Design of the Blended Wing Body Subsonic Transport. *J. Aircr.* **2004**, *41*, 10–25. [CrossRef]
9. Qin, N.; Vavalle, A.; le Moigne, A.; Laban, M.; Hackett, K.; Weinerfelt, P. Aerodynamic considerations of blended wing body aircraft. *Prog. Aerosp. Sci.* **2004**, *40*, 321–343. [CrossRef]
10. Hileman, J.I.; Spakovszky, Z.S.; Drela, M.; Sargeant, M.A.; Jones, A. Airframe Design for Silent Fuel-Efficient Aircraft. *J. Aircr.* **2010**, *47*, 956–969. [CrossRef]
11. Gohardani, A.S.; Doulgeris, G.; Singh, R. Challenges of future aircraft propulsion: A review of distributed propulsion technology and its potential application for the all electric commercial aircraft. *Prog. Aerosp. Sci.* **2011**, *47*, 369–391. [CrossRef]
12. Kim, H.D.; Felder, J.L.; Tong, M.T.; Armstrong, M. Revolutionary aeropropulsion concept for sustainable aviation: Turboelectric distributed propulsion. In Proceedings of the 2013 International Society for Air Breathing Engines, Busan, Korea, 9–13 September 2013.
13. Leifsson, L.; Ko, A.; Mason, W.H.; Schetz, J.A.; Grossman, B.; Haftka, R.T. Multidisciplinary design optimization of blended-wing-body transport aircraft with distributed propulsion. *Aerosp. Sci. Technol.* **2013**, *25*, 16–28. [CrossRef]
14. Lv, P.; Rao, A.G.; Ragni, D.; Veldhuis, L. Performance Analysis of Wake and Boundary-Layer Ingestion for Aircraft Design. *J. Aircr.* **2016**, *53*, 1517–1526. [CrossRef]
15. Hall, D.K.; Huang, A.C.; Uranga, A.; Greitzer, E.M.; Drela, M.; Sato, S. Boundary Layer Ingestion Propulsion Benefit for Transport Aircraft. *J. Propuls. Power* **2017**, *33*, 1118–1129. [CrossRef]
16. Uranga, A.; Drela, M.; Greitzer, E.M.; Hall, D.K.; Titchener, N.A.; Lieu, M.K.; Siu, N.M.; Casses, C.; Huang, A.C.; Gatlin, G.M.; et al. Boundary Layer Ingestion Benefit of the D8 Transport Aircraft. *AIAA J.* **2017**, *55*, 3693–3708. [CrossRef]
17. Blumenthal, B.T.; Elmiligui, A.A.; Geiselhart, K.A.; Campbell, R.L.; Maughmer, M.D.; Schmitz, S. Computational Investigation of a Boundary-Layer Ingesting Propulsion System for the Common Research Model. *J. Aircr.* **2019**, *55*, 1141–1153. [CrossRef] [PubMed]
18. Yildirim, A.; Gray, J.S.; Mader, C.A.; Martins, J.R.R.A. Boundary-Layer Ingestion Benefit for the STARC-ABL Concept. *J. Aircr.* **2022**, *59*, 896–911. [CrossRef]
19. Kerho, M.F. Aero-propulsive coupling of an embedded, distributed propulsion system. In Proceedings of the 33rd AIAA Applied Aerodynamics Conference, Dallas, TX, USA, 22–26 June 2015.
20. Schiltgen, B.T.; Freeman, J. Aeropropulsive interaction and thermal system integration within the ECO-150: A turboelectric distributed propulsion airliner with conventional electric machines. In Proceedings of the 16th AIAA Aviation Technology, Integration, and Operations Conference, Washington, DC, USA, 13–17 June 2016.
21. Perry, A.T.; Ansell, P.J.; Kerho, M.F. Aero-Propulsive and Propulsor Cross-Coupling Effects on a Distributed Propulsion System. *J. Aircr.* **2018**, *55*, 2414–2426. [CrossRef]
22. Yu, D.; Ansell, P.J.; Hristov, G. Aero-propulsive integration effects of an overwing distributed electric propulsion system. In Proceedings of the AIAA Scitech 2021 Forum, Virtual, 19–21 January 2021.

23. Borer, N.K.; Derlaga, J.M.; Deere, K.A.; Carter, M.B.; Viken, S.; Patterson, M.D.; Litherland, B.; Stoll, A. Comparison of aero-propulsive performance predictions for distributed propulsion configurations. In Proceedings of the 55th AIAA Aerospace Sciences Meeting, Grapevine, TX, USA, 9–13 January 2017.
24. Zhang, Y.; Zhou, Z.; Wang, K.; Fan, Z. Influences of distributed propulsion system parameters on aerodynamic characteristics of a BLI-BWB UAV. *Xibei Gongye Daxue Xuebao/J. Northwestern Polytech. Univ.* **2021**, *39*, 17–26. [CrossRef]
25. Zhang, X.; Zhang, W.; Li, W.; Zhang, X.; Lei, T. Experimental research on aero-propulsion coupling characteristics of a distributed electric propulsion aircraft. *Chin. J. Aeronaut.* 2022, *in press*. [CrossRef]
26. Drela, M. Power Balance in Aerodynamic Flows. *AIAA J.* **2009**, *47*, 1761–1771. [CrossRef]
27. Baskaran, P.; Corte, B.D.; van Sluis, M.; Rao, A.G. Aeropropulsive Performance Analysis of Axisymmetric Fuselage Bodies for Boundary-Layer Ingestion Applications. *AIAA J.* **2022**, *60*, 1592–1611. [CrossRef]